

# Current-density-modulated antiferromagnetic domain switching revealed by optical imaging in the Pt/CoO(001) bilayer

Tong Wu<sup>1</sup>, Haoran Chen,<sup>1</sup> Tianping Ma,<sup>2</sup> Jia Xu,<sup>3</sup> and Yizheng Wu<sup>1,4,5,\*</sup>

<sup>1</sup>Department of Physics and State Key Laboratory of Surface Physics, Fudan University, Shanghai 200433, China

<sup>2</sup>Anhui Key Laboratory of Magnetic Functional Materials and Devices, School of Materials Science and Engineering, Anhui University, Hefei 230601, China

<sup>3</sup>Department of Physics, School of Physics and Telecommunication Engineering, Shaanxi University of Technology, Hanzhong 723001, China

<sup>4</sup>Shanghai Research Center for Quantum Sciences, Shanghai 201315, China

<sup>5</sup>Shanghai Key Laboratory of Metasurfaces for Light Manipulation, Fudan University, Shanghai 200433, China

(Received 14 December 2023; revised 3 March 2024; accepted 5 April 2024; published 29 April 2024)

Efficient control of antiferromagnetic (AFM) domain switching in thin films is vital for advancing antiferromagnet-based memory devices. In this study, we directly observed the current-driven switching process of CoO AFM domains in the Pt/CoO(001) bilayer through the magneto-optical birefringence effect. The observed critical current density for AFM domain switching remains nearly constant across varying CoO thicknesses, associated with consistent switching polarity,  $\mathbf{n} \perp \mathbf{j}$ —where  $\mathbf{n}$  and  $\mathbf{j}$  stand for the Néel vector and current density vector, respectively—suggesting the dominance of the thermomagnetoelastic effect. Further confirmation comes from a similar switching process with  $\mathbf{n} \perp \mathbf{j}$  observed in the Pt/Al<sub>2</sub>O<sub>3</sub>/CoO sample, excluding the contribution of spin-current injection. Remarkably, it was also surprisingly observed that the Néel vector could be further switched parallel to the current direction ( $\mathbf{n} \parallel \mathbf{j}$ ) at higher current density. Our findings not only enhance our understanding of current-driven AFM domain switching but also present alternative avenues for manipulating AFM domains.

DOI: 10.1103/PhysRevApplied.21.044054

## I. INTRODUCTION

Antiferromagnetic (AFM) spintronics has attracted great attention in the past decade due to the unique characteristics of antiferromagnets, compared with ferromagnets, especially the absence of net magnetization producing no stray fields, making them inert to external fields and capable of serving as stable multilevel information storage media with high density [1–10]. Besides, their intrinsic precession frequency, which is determined by the exchange interaction, can reach as high as the terahertz (THz) level, allowing for ultrafast spin dynamics, such as THz pulse-induced AFM spin resonance [11,12]. It is noted that information stored in AFM spintronic devices is encoded in the Néel vector,  $\mathbf{n}$ , within AFM domains, making it imperative to image the AFM domains to understand their switching behaviors.

Up to now, x-ray magnetic linear dichroism (XMLD) effect based photoemission electron microscopy (PEEM) has been the prevailing technique for visualizing AFM domains in various AFM materials; this technique also allows changes to be observed after the application of an

external current or magnetic fields [5,6,13–17]. However, PEEM relies on the collected photoelectrons, making it challenging to concurrently capture the temporal evolution of AFM domains in the presence of an external field. Additionally, several other scanning imaging techniques, such as nitrogen-vacancy-center-based diamond microscopy and spin-polarized scanning tunneling microscopy, have been developed to measure the spin structure of antiferromagnets [18,19]. Yet, these approaches often necessitate a superflat surface and operate at low imaging speeds, limiting the real-time analysis of AFM domain-switching dynamics.

Recently, a method was proposed to image AFM domains based on the magneto-optical birefringence (MOB) effect, utilizing a tabletop commercial Kerr microscope [20,21]. This innovative technique enables wide-field imaging of AFM domains in thin films and has been validated in NiO(001) and CoO(001) single-crystal films grown on MgO(001) substrates [20,21]. More importantly, as a purely optical technique, it is compatible with current pulses and magnetic fields during the measurement process, allowing for the real-time investigation of AFM domain-switching behaviors under external fields [22,23].

\*Corresponding author: wuyizheng@fudan.edu.cn

The implementation of electrical manipulation of AFM domains is crucial in AFM spintronic devices, rendering the realization of the current-driven AFM domain switching and understanding the underlying mechanisms profoundly significant. For AFM metals, such as Mn<sub>2</sub>Au and CuMnAs, which exhibit broken local inversion symmetry in their crystal structures, have shown evidence of current-induced AFM domain switching through anisotropic magnetoresistance and XMLD-PEEM measurements [3–5, 24–26], and the switching mechanism was attributed to the spin-orbit-torque (SOT) effect [3,4]. The cases for AFM-insulator–heavy-metal systems, such as NiO/Pt, Fe<sub>2</sub>O<sub>3</sub>/Pt, and CoO/Pt, are much more complicated. It has been proved that spin Hall magnetoresistance (SMR) can be employed to detect the switching of AFM domains in these systems [7,27,28]. However, the measured magnetoresistance signal was then proved not necessarily to have a one-to-one correspondence with the state of AFM domains [29]. Further investigations with domain imaging based on the MOB effect confirmed current-driven switching of AFM domains in the NiO/Pt bilayer, verifying the capacity of the MOB effect to study the dynamics of AFM domain switching in the presence of external fields [23,30]. In such systems, the underlying mechanism of current-driven AFM domain switching was initially explained by the anti-dampinglike SOT effect in NiO/Pt [7,8]. Subsequently, the thermomagnetoelastic effect was proposed to explain the current-driven AFM domain switching in Fe<sub>2</sub>O<sub>3</sub>/Pt [27], and this explanation was further applied to understand the phenomenon in NiO/Pt using optical imaging [30].

CoO is a common collinear *G*-type antiferromagnet with AFM spins aligning along the (111) directions in its bulk phase with a Néel temperature ( $T_N$ ) of 291 K [31]. Because the lattice constant of CoO is slightly larger than that of MgO ( $a_{\text{CoO}} = 4.26 \text{ \AA} > a_{\text{MgO}} = 4.21 \text{ \AA}$ ), the epitaxial CoO(001) thin film on the MgO(001) substrate undergoes in-plane compressive strain, leading to an in-plane biaxial spin alignment along the [110] and [−110] directions and a higher  $T_N$  of about 310 K due to strong magnetoelastic coupling [32,33]. The presence of two available in-plane states for AFM domains, combined with the relatively low  $T_N$ , makes it suitable for the development of energy-efficient information-storage devices under ambient conditions. Previous studies have shown AFM domain switching in CoO/Pt, induced by either a current or a field, as investigated by the SMR effect [28,34–36] or XMLD signal [35,36]. However, current-driven domain switching in CoO has not been confirmed by direct imaging yet, and the exact switching mechanism still remains elusive [28]. Here, we demonstrate the current-driven AFM domain switching in the Pt/CoO(001) bilayer by optical imaging. Systematic measurements with variable temperatures and CoO thicknesses were also performed. The measured critical current density was found to be almost independent of CoO thickness and the same switching polarity,

with  $\mathbf{n} \perp \mathbf{j}$ , was observed at various temperatures and CoO thicknesses. Combined with similar reversible switching in the sample with a 4-nm Al<sub>2</sub>O<sub>3</sub> spacer layer between CoO and Pt layers, it was confirmed that the current-driven switching of the CoO AFM domains should be attributed to the thermomagnetoelastic effect. Furthermore, it was surprisingly discovered that AFM domains in CoO could further align parallel to the direction of the current ( $\mathbf{n} \parallel \mathbf{j}$ ) at higher current density, which was distinct from their behavior at lower current density ( $\mathbf{n} \perp \mathbf{j}$ ). This finding allows domain-orientation manipulation by different current densities instead of current directions.

## II. EXPERIMENTS

Single-crystalline CoO(001) films were prepared by molecular beam epitaxy in an ultrahigh vacuum system with a base pressure of  $2 \times 10^{-10}$  Torr. The CoO layer was grown on the preannealed single-crystal MgO(001) substrate by reactive deposition of Co at an oxygen pressure of  $4 \times 10^{-6}$  Torr at room temperature. To verify whether the spin current transmitted through the Pt/CoO interface plays a role in the switching process, it is necessary to study the CoO thickness dependence of the current-driven switching process. Thus, the CoO layer was grown as a wedge, ranging from 0 to 8 nm, with a length of 6 mm by moving the sample holder behind a shield during deposition, as shown in Fig. 1(a). Epitaxial growth of the CoO layer is evident from the sharp reflection high-energy electron-diffraction patterns in Figs. 1(b) and 1(c), which confirm the lattice relationship of CoO[100](001)/MgO[100](001). Then, the sample was transferred to the magnetron sputtering system and a 3-nm-thick Pt layer was deposited. Finally, through standard lithography and Ar<sup>+</sup>-etching processes, the sample was patterned into 10-μm-wide cross bars with the arms of the devices along two easy axes of CoO, i.e., [110] and [−110].

We then investigated the current-driven AFM domain switching using a commercial Kerr microscope equipped with an optical cryostat, allowing operation within a temperature range between 77 K and room temperature, as illustrated in Fig. 1(d). The CoO AFM domains were imaged with blue light incident normal to the sample. The polarization of incident light is parallel to the (100) direction, ensuring the strongest MOB contrast for the AFM domains [20]. To perform studies on the current-driven AFM domain switching, current pulses with the duration of 100 μs were applied. The pulses were applied through a Keithley 6221 current source and were switched between the [110] and [−110] directions of CoO. The samples were initialized by applying strong currents along a certain direction to form a single AFM domain. Subsequently, the current pulses were applied in the direction perpendicular to the initial currents, gradually increasing the current density. The CoO AFM domains were imaged

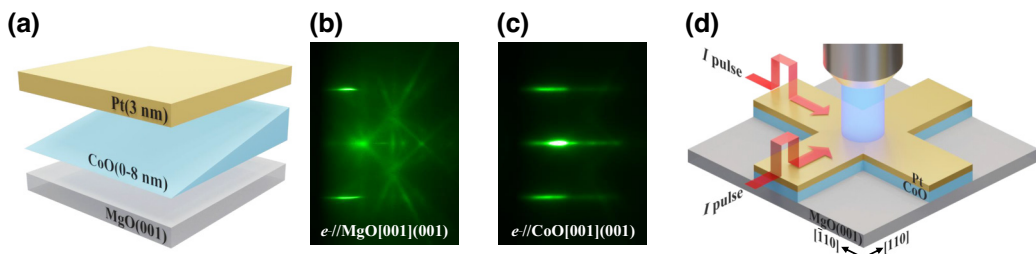


FIG. 1. (a) Structure of the Pt/CoO(001) sample with the CoO layer grown as a wedge shape. RHEED patterns of (b) MgO(001) substrate and (c) 8-nm CoO(001) film. (d) Schematic illustration of the MOB setup with the crossbar structure.

1 s after each current pulse, with an exposure time of about 1 s for imaging. After the application of current pulses, the ratios of switched AFM domains were determined from the MOB images at the crossing area within the devices, as indicated by the red dashed box in Fig. 2(a).

### III. RESULTS AND DISCUSSION

Figures 2(a)–2(d) illustrate the AFM domain-switching process in an 8-nm-thick CoO device measured at 80 K with current pulses along the  $-y$  direction, as indicated by

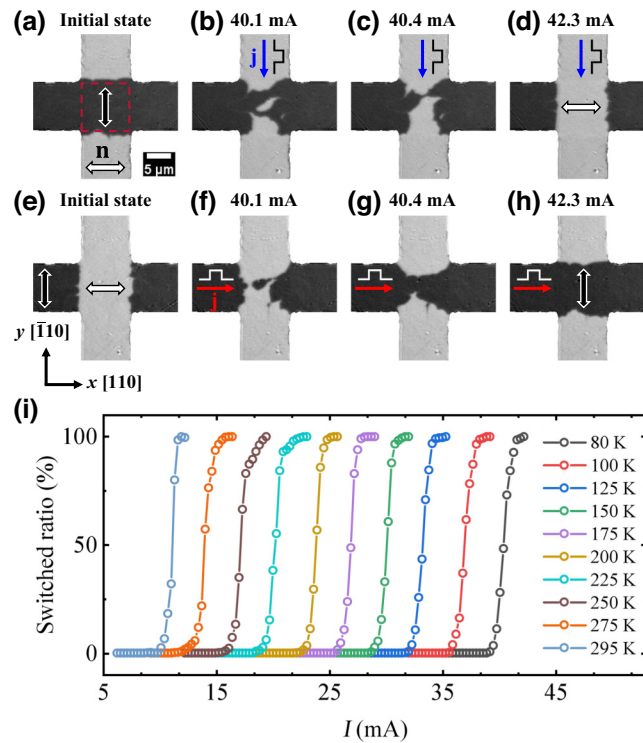


FIG. 2. (a) Initial state with  $\mathbf{n} \parallel y$  axis at the cross. (b)–(d) Intermediate states after pulses along the  $-y$  direction with increasing current densities. (e) Initial state with  $\mathbf{n} \parallel x$  axis in the cross area. (f)–(h) Intermediate states after pulses along the  $+x$  direction with increasing current densities. (i) Switching curves of 8-nm CoO at different temperatures.

the blue arrows. Figure 2(a) shows the initial state with the Néel vector,  $\mathbf{n}$ , of CoO at the center of the device along the  $y$  axis after applying a strong current along the  $+x$  direction. The relationship between the direction of  $\mathbf{n}$  and the optical contrast was first characterized in the Fe/CoO(001) film, demonstrating orthogonal coupling between the Fe spins and CoO AFM spins [21]. Figures 2(b)–2(d) represent the intermediate states during the switching process after the pulses with increasing current strengths. The states during the switching process with orthogonal current pulses are also presented in Figs. 2(e)–2(h). Figure 2(e) shows the state with  $\mathbf{n}$  at the cross aligned along the  $x$  axis. Figures 2(f)–2(h) show the intermediate states after the current pulses applied in the bar along the  $+x$  direction, as indicated by the red arrows. Clear and reversible switching of the AFM domain was observed with a polarity of  $\mathbf{n} \perp \mathbf{j}$  after switching. During the switching process, both domain nucleation and domain-wall motion could be observed. Similar measurements were conducted at different temperatures, ranging from 80 K to room temperature. We then determined the relationship between the switched ratio of the AFM domain and the current density along the  $y$  axis at different temperatures. The switching curves in Fig. 2(i) confirm 100% switching at all temperatures but shift towards lower current density, while maintaining the similar shape, as the temperature increases.

We also imaged AFM domain switching with different CoO thicknesses ( $d_{\text{CoO}}$ ), as depicted in Fig. 3, at 80 K. Figures 3(a)–3(d) exhibit the final states of CoO films with different  $d_{\text{CoO}}$  after current pulses applied along the  $+x$  direction, while Figs. 3(e)–3(h) show the final states after current pulses applied along the  $-y$  direction. The optical contrast of the AFM domains increases with increasing  $d_{\text{CoO}}$ , owing to the thickness dependence of the MOB effect in the CoO film [21]. All CoO films with different thicknesses show the same switching polarity of  $\mathbf{n} \perp \mathbf{j}$ , implying the same switching mechanism independent of film thickness. Figure 3(i) shows the measured switching curves with different  $d_{\text{CoO}}$  at 80 K, which have very weak thickness dependence on AFM domain switching. The critical current density of switching curves vary by approximately 1.8% across CoO thicknesses ranging from 3 to 8 nm. Even

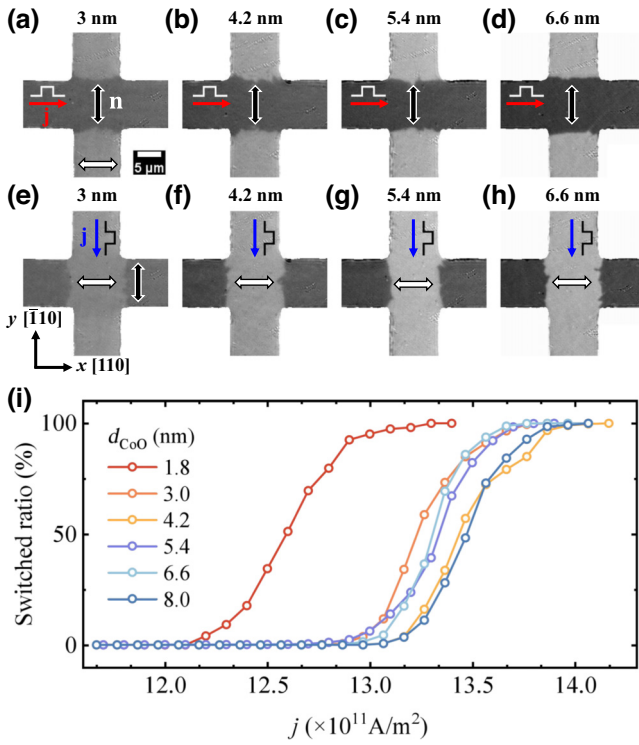


FIG. 3. (a)–(d) Final states with  $\mathbf{n} \parallel y$  axis, and (e)–(h) final states with  $\mathbf{n} \parallel x$  axis at the cross with different CoO thicknesses after the current pulses applied in different bars. Current pulses are indicated by the red or blue arrows in each image. (i) Switching curves at 80 K with different CoO thicknesses.

in the case of the 1.8-nm-thick CoO film, the switching current density is only about 4% lower than devices with thicker films.

To quantitatively investigate the impact of temperature and CoO thickness on the current-driven AFM domain-switching process, the critical current densities ( $j_c$ ) were extracted from the switching curves with different  $d_{\text{CoO}}$  at various temperatures, as illustrated in Figs. 4(a) and 4(b), where  $j_c$  signifies the current density with a 50% switched ratio. For the device with 1.8-nm-thick CoO, the contrast of AFM domains is too weak to be distinguished above 125 K. For the devices with  $d_{\text{CoO}}$  ranging from 3 to 5.4 nm, the switched ratio at high temperatures cannot exceed 50%, possibly due to the current-induced random thermal excitation overcoming the anisotropy barrier, resulting in a multidomain state. At a fixed temperature,  $j_c$  remains nearly independent of  $d_{\text{CoO}}$ . This observation suggests an origin of AFM domain switching that does not rely on the interface, which would typically weaken with increased thickness. Conversely, with a fixed  $d_{\text{CoO}}$ ,  $j_c$  exhibits a linear decrease as the temperature increases, as depicted in Fig. 4(b). It was reported that the Joule-heating-induced temperature increase,  $\Delta T$ , was proportional to  $j^2$  [27], and the magnetic anisotropy of the AFM CoO film was also reduced due to the increasing temperature. Thus, the linear

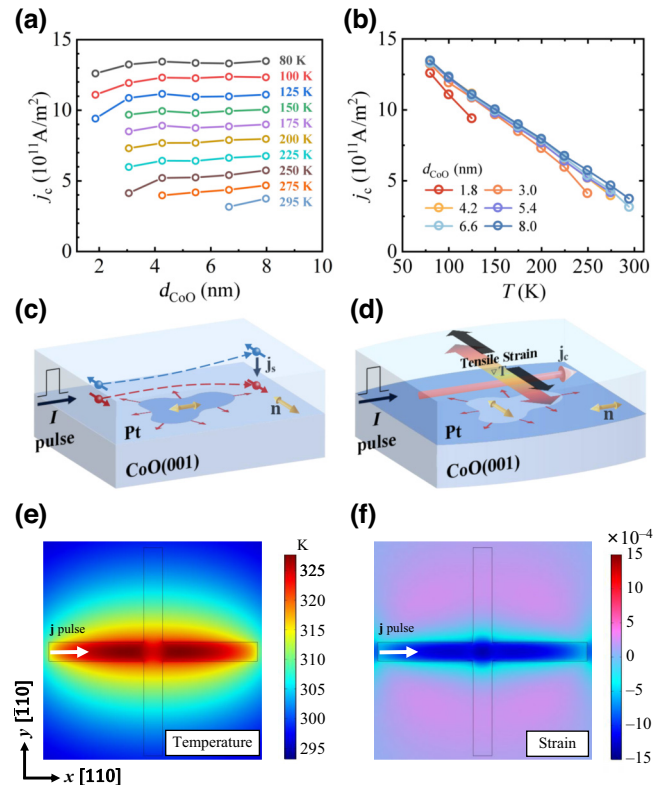


FIG. 4. (a) Switching current density,  $j_c$ , as a function of  $d_{\text{CoO}}$  at different temperatures. (b) Switching current density,  $j_c$ , as a function of temperature with different  $d_{\text{CoO}}$ . (c) Schematic diagram of the SOT-induced switching mechanism. (d) Schematic diagram of the thermomagnetoelastic-effect-induced switching mechanism. (e) Temperature and (f) strain distribution simulated after applying the current pulse with a width of 100  $\mu\text{s}$  and an amplitude of 15 mA.

relationship between  $j_c$  and temperature here should not only be attributed to the Joule-heating-induced temperature increase but may also arise from the reduction of the switching-energy barrier of CoO due to thermal excitation. Figure 4(b) also shows that the relationships between critical current density and temperature for different  $d_{\text{CoO}}$  are concentrated within a narrow range, due to the weak  $d_{\text{CoO}}$  dependence on the switching process shown in Fig. 4(a). While decreasing the temperature,  $j_c$  increases from about  $3.1 \times 10^{11} \text{ A/m}^2$  at 295 K to about  $13.3 \times 10^{11} \text{ A/m}^2$  at 80 K.

Next, we further discuss the physical mechanisms governing current-driven AFM domain switching in the Pt/CoO bilayer. Regarding current-driven AFM domain switching in the heavy-metal–AFM-insulator heterostructure, two mechanisms have been proposed. One is anti-dampinglike SOT resulting from the spin current generated in the heavy-metal layer [7,8], capable of aligning the Néel vector parallel to the current direction ( $\mathbf{n} \parallel \mathbf{j}$ ), as depicted

in Fig. 4(c). The other mechanism involves the Joule-heating-induced magnetoelastic coupling effect induced by the current pulse [27,28,30]. Because of the Joule heating generated by the applied current pulse, the current path experiences a higher temperature than the surrounding substrate. Consequently, greater thermal expansion occurs at the central current path, leading to a net tensile strain perpendicular to the current direction, as illustrated in Fig. 4(d). Such tensile strain can induce in-plane uniaxial anisotropy in the AFM layer due to the magnetoelastic coupling effect, which can further drive the AFM spins towards the easy axis during the cooling process after the current pulse. The magnetic energy introduced by the Joule-heating-induced magnetoelastic coupling scales as  $E \propto -\lambda(\mathbf{n} \cdot \mathbf{j})^2$  [28], where  $\lambda$  stands for the magnetoelastic coefficient. Therefore, a positive  $\lambda$  signifies the parallel alignment of the final AFM spins with the current direction, i.e.,  $\mathbf{n} \parallel \mathbf{j}$ , whereas a negative  $\lambda$  results in AFM spins perpendicular to the current, as indicated by the relationship  $\mathbf{n} \perp \mathbf{j}$ . The current-induced switching effect in Pt/CoO cannot be explained by the antidampinglike SOT effect, since the observed final state of AFM domains follows the relationship of  $\mathbf{n} \perp \mathbf{j}$ , which is in line with the thermomagnetoelastic switching mechanism for a negative magnetoelastic constant of CoO [28]. Our findings, exploring current-induced switching as a function of temperature and  $d_{\text{CoO}}$ , strongly support the thermomagnetoelastic switching mechanism. Notably, the critical current density remains independent of  $d_{\text{CoO}}$ , excluding the mechanism associated with the SOT effect, which typically exhibits a significant thickness dependence. However, the thermal-induced strain is mainly determined by the insulating substrate and the metallic current line and has no direct correlation with the CoO film. In this case, the thermomagnetoelastic switching mechanism should have no dependence on the CoO thickness.

To further verify the thermomagnetoelastic switching mechanism, we conducted simulations using COMSOL following the methods described in Refs. [27,28,30]. Modeling was performed based on the crossbar device with real dimensions, such as a length of 110  $\mu\text{m}$  and width of 10  $\mu\text{m}$ , as indicated in Fig. 4(e). The thicknesses of the Pt and CoO layers were set as 3 and 8 nm, respectively. The MgO substrate was modeled with dimensions of 1 mm  $\times$  1 mm  $\times$  10  $\mu\text{m}$ . We chose the same boundary conditions and material parameters, such as heat capacity, thermal conductivity, and heat-transfer coefficient, as in Refs. [28,30]. A pulse current with a width of 100  $\mu\text{s}$  and an amplitude of 15 mA was injected into the arm along the  $+x$  direction at 295 K, then the thermal and strain distributions at the bottom surface of the CoO layer were calculated as a function of time. Figure 4(e) shows that the temperature in the current path at a time of 100  $\mu\text{s}$  significantly exceeds that of the surrounding substrate, reaching an instantaneous maximum of 320 K, closely approaching

the  $T_N$  of CoO film. The nonuniform temperature distribution within the film will further generate strain. The lower temperature in the cross area can be attributed to the higher heat-transfer rate in the Pt bars perpendicular to the current. However, the relatively lower temperature near the end of the current-carrying electrode is due to the additional heat-dissipation boundary at the end of the device, as heat generation mainly occurs within the device. In the actual experimental setup, the end was connected to a larger and thicker electrode area for wire bonding, resulting in decreased current density and a naturally lower temperature in this area. Figure 4(f) presents the calculated distribution of the net tensile strain defined as  $\varepsilon_{xx} - \varepsilon_{yy}$ , with  $\varepsilon_{xx}$  and  $\varepsilon_{yy}$  as the strain along the  $x$  and  $y$  axes, respectively. The positive or negative values of  $\varepsilon_{xx} - \varepsilon_{yy}$  correspond to the net tensile strain along the  $x$  or  $y$  axes, respectively. Thus, the calculated negative net tensile strain shown in Fig. 4(f) can induce uniaxial anisotropy with the easy axis along the  $y$  axis due to the negative magnetoelastic constant. Note that the maximum temperature after the current pulse can reach the  $T_N$  of CoO film, thus, during the cooling process, the magnetoelastic-effect-induced uniaxial anisotropy can drive the AFM spins along the  $y$  axis. At lower experimental temperatures, achieving a sufficiently high sample-temperature change for AFM domain switching requires a higher current strength, as shown in Fig. 2(i). Therefore, our numerical simulations further corroborate the dominance of the thermomagnetoelastic effect in the CoO/Pt bilayer for AFM domain switching. It should be noted that, in the time-dependent simulations, the strain-relaxation rate is much faster than the temperature-relaxation rate. For example, while performing the simulation with a current of 35 mA at 295 K, the sample temperature can still remain above 315 K at 0.3 ms after the current pulse, whereas the strain is negligible, being 3 orders of magnitude smaller than its peak value. Thus, the paramagnetic-AFM phase transition occurs under conditions of nearly zero strain distribution, potentially leading to the random distribution of AFM domains due to the fourfold symmetry in the CoO(001) film.

While further increasing the current density, we observed an additional domain switching with the final state of  $\mathbf{n} \parallel \mathbf{j}$ . Figure 5(a) shows the switching curves and the domain states at several characteristic current densities at the cross area of the device with the 8-nm-thick CoO film, as a function of current density for the current pulses applied along two bars. The white and black contrasts denote  $\mathbf{n}$  along the  $x$  and  $y$  axes, respectively, as indicated by the double arrows. For  $\mathbf{j} \parallel [\bar{1}10](-y \text{ axis})$ , the domain switched to the white-contrast state of  $\mathbf{n} \perp \mathbf{j}$  at a critical current density of  $j_c \sim 4.6 \times 10^{11} \text{ A/m}^2$ . However, it also revealed an additional domain switching with the final black-contrast state of  $\mathbf{n} \parallel \mathbf{j}$  at a higher critical current density of  $j_{hc} \sim 9.8 \times 10^{11} \text{ A/m}^2$ . For  $\mathbf{j} \parallel [110](+x \text{ axis})$ ,

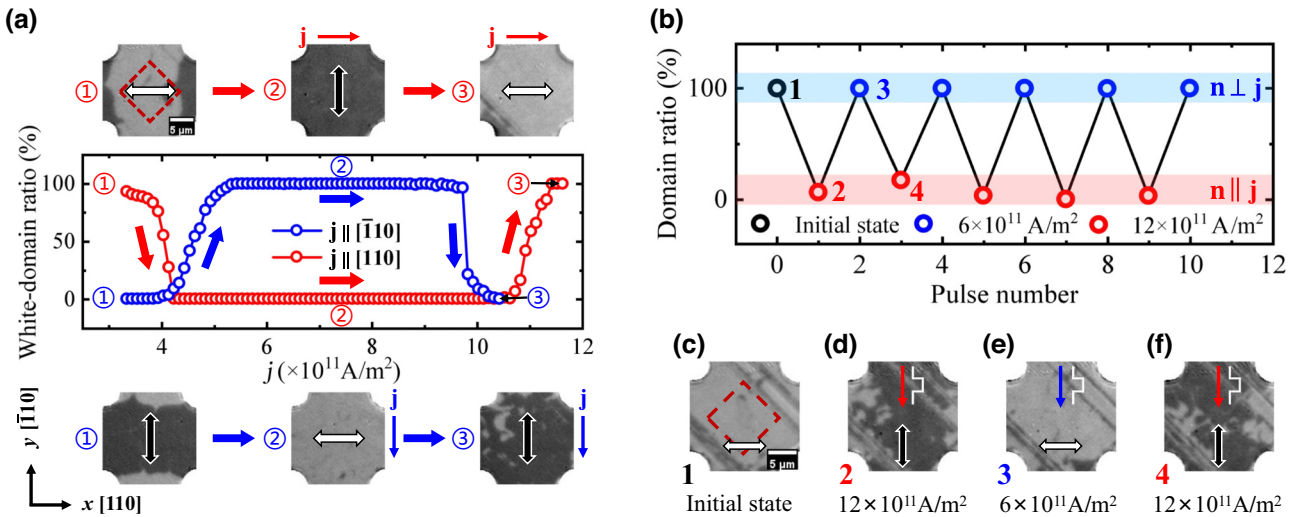


FIG. 5. (a) Switching curves for 8-nm CoO measured at 275 K with  $j \parallel [\bar{1}10]$  ( $-y$ ) (blue hollow point line) and  $j \parallel [110]$  ( $x$ ) (red hollow point line), respectively. Insets illustrate the AFM domain states at several characteristic current densities. (b) Ratio of AFM domain states with the AFM spins along [110] direction after applying the current pulses with alternating magnitude. (c)–(f) Initial state and states after current pulses with the current densities of  $12 \times 10^{11} \text{ A/m}^2$  (red arrow) and  $6 \times 10^{11} \text{ A/m}^2$  (blue arrow), respectively, corresponding with the states marked by the numbers in (b). Evolution of the domain ratio was determined in the center area of the cross marked by the red dashed squares in (a) and (c).

similar two-step switching behavior can also be observed with critical current densities of  $j_c \sim 4.1 \times 10^{11} \text{ A/m}^2$  and  $j_{hc} \sim 11.0 \times 10^{11} \text{ A/m}^2$ . The current-induced switching for  $j \parallel [110]$  exhibits a lower  $j_c$  but a higher  $j_{hc}$ . It is possible that the CoO film has a weak in-plane uniaxial anisotropy with an easy axis along  $[\bar{1}10]$ , which can be induced by the possible small miscut of MgO(001) substrate [37].

The results in Fig. 5(a) provide an unconventional opportunity to switch the AFM domains by different current densities. We applied two distinct currents along the  $x$  axis, with densities,  $j$ , of  $6 \times 10^{11} \text{ A/m}^2$  ( $j_c < j < j_{hc}$ ) and  $12 \times 10^{11} \text{ A/m}^2$  ( $j > j_{hc}$ ), and measured the MOB signal at the cross area. Figure 5(b) clearly shows the alternating changes in domain contrast induced by these two varied currents. Figures 5(c)–5(f) show representative domain images after current pulses with alternating strengths, which clearly demonstrate different switching by current pulses with different densities. This result highlights the potential for achieving reversible switching of AFM domains by adjusting the current density in a simple two-terminal device, deviating from the traditional method of altering the current direction in a four-terminal device with a crossbar structure [28].

The mechanism for CoO AFM domain switching to the state of  $n \parallel j$  at high current density remains unclear. Our numerical simulations indicate that the current pulses consistently induce net tensile strain perpendicular to the current direction, regardless of current density. The temperature tends to stabilize quickly, with an increase of less than 3 K at 2 ms after the current pulse compared to the initial temperature, even with a strong current of 35 mA. The

transient strain stabilizes even faster, almost disappearing within 1 ms. Thus, the ordinary magnetoelastic effect can only account for the AFM domain switching into the state of  $n \perp j$ . It is noted that the antidampinglike SOT effect can induce the final state with  $n \parallel j$  [7,8], suggesting the possibility that additional switching at a higher current density may be influenced by the spin current from the Pt layer. To investigate the influence of the spin current from the Pt layer, we inserted a 4-nm-thick Al<sub>2</sub>O<sub>3</sub> layer into the Pt/CoO bilayer, aimed at blocking the injection of spin current from the Pt layer to the CoO layer. As a result, this configuration should effectively eliminate the possible SOT effect in the system, as illustrated in Fig. 6(a). We conducted similar current-driven AFM domain-switching measurements on a Pt(3 nm)/Al<sub>2</sub>O<sub>3</sub>(4 nm)/CoO(8 nm) sample. Our measurements first demonstrated that the same current-induced AFM domain switching with  $n \perp j$  could be achieved at low current density, as shown in Figs. 6(b) and 6(c). This result is consistent with the switching mechanism of the thermomagnetoelastic effect. However, upon further increasing the current strength, the second current-induced domain switching with  $n \parallel j$  could also be observed. Remarkably, this alternate switching can be triggered by currents of two different densities, as evidenced by the domain images in Figs. 6(d)–6(g). Hence, domain switching at high current density above  $j_{hc}$  in the Pt/Al<sub>2</sub>O<sub>3</sub>/CoO sample effectively excludes the likelihood of its origin from the SOT effect. This additional switching might also be attributed to the thermomagnetoelastic effect induced by the current pulse. Our numerical simulations indicate that the current pulse with  $j = 12 \times 10^{11} \text{ A/m}^2$

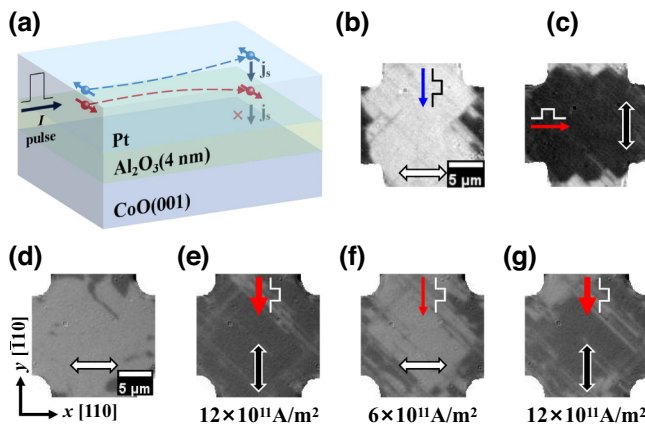


FIG. 6. (a) Schematic diagram illustrating the blocking effect of the  $\text{Al}_2\text{O}_3$  interlayer on the injection of spin current from the Pt layer to the CoO layer. States after current pulses along (b)  $-y$  and (c)  $+x$  directions. (d) Initial state with  $\mathbf{n} \parallel x$  axis at the device center. (e)–(g) Final states after current pulses with different magnitudes.

can elevate the temperature at the device center to about 470 K from room temperature, which is far above the  $T_N$  of CoO film. Thus, the heat-conduction process may be nonlinear and anisotropic in the crystalline system, which is beyond the capability of the conventional numerical simulation method employed in this study. It should also be noted that when a large current is applied to induce AFM domain switching with  $\mathbf{n} \parallel \mathbf{j}$ , strain could lead to the formation of gridlike defects in the sample oriented along the  $\langle 100 \rangle$  direction, as shown in Figs. 5(e)–5(f) and 6(e)–6(g), potentially restricting the switching numbers. Although the mechanism of the current-induced switching of CoO AFM domains at high current density remains unclear, our findings demonstrate the possibility to reversibly manipulate the AFM domains only by adjusting the current density instead of changing the direction of the current. This feature can promote the development of a two-terminal device that has the potential to simplify the complexity of antiferromagnet-based devices.

#### IV. SUMMARY

We systematically investigated the current-driven switching of AFM domains in the Pt/CoO(001) system through direct optical imaging, considering various temperatures, CoO thicknesses, and different strengths of current pulses. We discovered that the critical current density,  $j_c$ , for AFM domain switching was independent of the CoO thickness. Furthermore, different CoO thicknesses and temperatures yield the same switching polarity with  $\mathbf{n} \perp \mathbf{j}$ . Our results suggest that AFM domain switching in the CoO/Pt bilayer is dominated by the thermomagnetoelastic effect, and this conclusion is further supported by simulation results. The analogous switching process

observed with  $\mathbf{n} \perp \mathbf{j}$  in the Pt/Al<sub>2</sub>O<sub>3</sub>/CoO sample further rules out the possibility of the SOT effect contributing to the phenomenon. The observation of additional domain switching with  $\mathbf{n} \parallel \mathbf{j}$  at a higher current density, while maintaining the same current direction, indicates the potential to manipulate AFM domains in a two-terminal device solely by adjusting the current density. Our experimental investigation not only offers a deeper understanding of current-driven AFM domain switching but also unveils prospects for manipulating AFM domains in AFM spintronic devices.

#### ACKNOWLEDGMENTS

The work was supported by the National Key Research and Development Program of China (Grant No. 2022YFA1403300), the National Natural Science Foundation of China (Grants No. 11974079, No. 12274083, and No. 12221004), the Shanghai Municipal Science and Technology Major Project (Grant No. 2019SHZDZX01), and the Shanghai Municipal Science and Technology Basic Research Project (Grants No. 22JC1400200 and No. 23dz2260100). J.X. acknowledges support from the National Natural Science Foundation of China (Grant No. 12204295), the Natural Science Foundation of Shaanxi Provincial Department of Education (Grant No. 22JK0310), the Natural Science Basic Research Program of Shaanxi (Grant No. 2022JQ-017), Shaanxi University of Technology (Grant No. SLGRCQD2125), and the Youth Hanjiang Scholar Research Support Fund from Shaanxi University of Technology.

*Note added.*—Recently, we became aware of the related work of Ref. [38], in which XMLD-PEEM was utilized to investigate AFM domain switching in the Pt/CoO system induced by the nonuniform current passing through the neighboring arms of a cross bar. It was claimed that both the thermomagnetoelastic effect and the SOT effect contributed to the AFM domain switching.

- [1] A. H. MacDonald and M. Tsui, Antiferromagnetic metal spintronics, *Philos. Trans. R. Soc., A* **369**, 3098 (2011).
- [2] T. Jungwirth, X. Martí, P. Wadley, and J. Wunderlich, Antiferromagnetic spintronics, *Nat. Nanotechnol.* **11**, 231 (2016).
- [3] P. Wadley, *et al.*, Electrical switching of an antiferromagnet, *Science* **351**, 587 (2016).
- [4] S. Yu. Bodnar, L. Šmejkal, I. Turek, T. Jungwirth, O. Gomonay, J. Sinova, A. A. Sapozhnik, H.-J. Elmers, M. Kläui, and M. Jourdan, Writing and reading antiferromagnetic Mn<sub>2</sub>Au by Néel spin-orbit torques and large anisotropic magnetoresistance, *Nat. Commun.* **9**, 348 (2018).
- [5] P. Wadley, S. Reimers, M. J. Grzybowski, C. Andrews, M. Wang, J. S. Chauhan, B. L. Gallagher, R. P. Campion, K. W. Edmonds, S. S. Dhesi, F. Maccherozzi,

- V. Novak, J. Wunderlich, and T. Jungwirth, Current polarity-dependent manipulation of antiferromagnetic domains, *Nat. Nanotechnol.* **13**, 362 (2018).
- [6] T. Moriyama, K. Oda, T. Ohkochi, M. Kimata, and T. Ono, Spin torque control of antiferromagnetic moments in NiO, *Sci. Rep.* **8**, 14167 (2018).
- [7] X. Z. Chen, R. Zarzuela, J. Zhang, C. Song, X. F. Zhou, G. Y. Shi, F. Li, H. A. Zhou, W. J. Jiang, F. Pan, and Y. Tserkovnyak, Antidamping-torque-induced switching in biaxial antiferromagnetic insulators, *Phys. Rev. Lett.* **120**, 207204 (2018).
- [8] L. Baldrati, O. Gomonay, A. Ross, M. Filianina, R. Lebrun, R. Ramos, C. Leveille, F. Fuhrmann, T. R. Forrest, F. Maccherozzi, S. Valencia, F. Kronast, E. Saitoh, J. Sinova, and M. Kläui, Mechanism of Néel order switching in antiferromagnetic thin films revealed by magnetotransport and direct imaging, *Phys. Rev. Lett.* **123**, 177201 (2019).
- [9] D. Kriegner, K. Výborný, K. Olejník, H. Reichlová, V. Novák, X. Marti, J. Gazquez, V. Saidl, P. Němec, V. V. Volobuev, G. Springholz, V. Holý, and T. Jungwirth, Multiple-stable anisotropic magnetoresistance memory in antiferromagnetic MnTe, *Nat. Commun.* **7**, 11623 (2016).
- [10] K. Olejník, V. Schuler, X. Marti, V. Novák, Z. Kašpar, P. Wadley, R. P. Campion, K. W. Edmonds, B. L. Gallagher, J. Garces, M. Baumgartner, P. Gambardella, and T. Jungwirth, Antiferromagnetic CuMnAs multi-level memory cell with microelectronic compatibility, *Nat. Commun.* **8**, 15434 (2017).
- [11] T. Kampfrath, A. Sell, G. Klatt, A. Pashkin, S. Mährlein, T. Dekorsy, M. Wolf, M. Fiebig, A. Leitenstorfer, and R. Huber, Coherent terahertz control of antiferromagnetic spin waves, *Nat. Photonics* **5**, 31 (2011).
- [12] N. Bhattacharjee, A. A. Sapozhnik, S. Yu. Bodnar, V. Yu. Grigorev, S. Y. Agustsson, J. Cao, D. Dominko, M. Obergfell, O. Gomonay, J. Sinova, M. Kläui, H.-J. Elmers, M. Jourdan, and J. Demsar, Néel spin-orbit torque driven antiferromagnetic resonance in Mn<sub>2</sub>Au probed by time-domain THz spectroscopy, *Phys. Rev. Lett.* **120**, 237201 (2018).
- [13] J. Stöhr, A. Scholl, T. J. Regan, S. Anders, J. Lüning, M. R. Scheinfein, H. A. Padmore, and R. L. White, Images of the antiferromagnetic structure of a NiO(100) surface by means of x-ray magnetic linear dichroism spectromicroscopy, *Phys. Rev. Lett.* **83**, 1862 (1999).
- [14] A. A. Sapozhnik, M. Filianina, S. Yu. Bodnar, A. Lamirand, M.-A. Mawass, Y. Skourski, H.-J. Elmers, H. Zabel, M. Kläui, and M. Jourdan, Direct imaging of antiferromagnetic domains in Mn<sub>2</sub>Au manipulated by high magnetic fields, *Phys. Rev. B* **97**, 134429 (2018).
- [15] F. Nolting, A. Scholl, J. Stöhr, J. W. Seo, J. Fompeyrine, H. Siegwart, J.-P. Locquet, S. Anders, J. Lüning, E. E. Fullerton, M. F. Toney, M. R. Scheinfein, and H. A. Padmore, Direct observation of the alignment of ferromagnetic spins by antiferromagnetic spins, *Nature* **405**, 767 (2000).
- [16] H. Ohldag, A. Scholl, F. Nolting, S. Anders, F. U. Hillebrecht, and J. Stöhr, Spin reorientation at the antiferromagnetic NiO(001) surface in response to an adjacent ferromagnet, *Phys. Rev. Lett.* **86**, 2878 (2001).
- [17] F. Kronast, J. Schlichting, F. Radu, S. K. Mishra, T. Noll, and H. A. Dürr, Spin-resolved photoemission microscopy and magnetic imaging in applied magnetic fields, *Surf. Interface Anal.* **42**, 1532 (2010).
- [18] I. Gross, W. Akhtar, V. Garcia, L. J. Martínez, S. Chouaib, K. Garcia, C. Carrétéro, A. Barthélémy, P. Appel, P. Maletinsky, J.-V. Kim, J. Y. Chauleau, N. Jaouen, M. Viret, M. Bibes, S. Fusil, and V. Jacques, Real-space imaging of non-collinear antiferromagnetic order with a single-spin magnetometer, *Nature* **549**, 252 (2017).
- [19] M. Bode, E. Y. Vedmedenko, K. Von Bergmann, A. Kubetzka, P. Ferriani, S. Heinze, and R. Wiesendanger, Atomic spin structure of antiferromagnetic domain walls, *Nat. Mater.* **5**, 477 (2006).
- [20] J. Xu, C. Zhou, M. Jia, D. Shi, C. Liu, H. Chen, G. Chen, G. Zhang, Y. Liang, J. Li, W. Zhang, and Y. Wu, Imaging antiferromagnetic domains in nickel oxide thin films by optical birefringence effect, *Phys. Rev. B* **100**, 134413 (2019).
- [21] J. Xu, H. Chen, C. Zhou, D. Shi, G. Chen, and Y. Wu, Optical imaging of antiferromagnetic domains in ultrathin CoO(001) films, *New J. Phys.* **22**, 083033 (2020).
- [22] J. Xu, J. Xia, X. Zhang, C. Zhou, D. Shi, H. Chen, T. Wu, Q. Li, H. Ding, Y. Zhou, and Y. Wu, Exchange-torque-triggered fast switching of antiferromagnetic domains, *Phys. Rev. Lett.* **128**, 137201 (2022).
- [23] F. Schreiber, L. Baldrati, C. Schmitt, R. Ramos, E. Saitoh, R. Lebrun, and M. Kläui, Concurrent magneto-optical imaging and magneto-transport readout of electrical switching of insulating antiferromagnetic thin films, *Appl. Phys. Lett.* **117**, 082401 (2020).
- [24] J. Godinho, H. Reichlová, D. Kriegner, V. Novák, K. Olejník, Z. Kašpar, Z. Šobáň, P. Wadley, R. P. Campion, R. M. Otxoa, P. E. Roy, J. Železný, T. Jungwirth, and J. Wunderlich, Electrically induced and detected Néel vector reversal in a collinear antiferromagnet, *Nat. Commun.* **9**, 4686 (2018).
- [25] V. Saidl, P. Němec, P. Wadley, V. Hills, R. P. Campion, V. Novák, K. W. Edmonds, F. Maccherozzi, S. S. Dhesi, B. L. Gallagher, F. Trojánek, J. Kuneš, J. Železný, P. Malý, and T. Jungwirth, Optical determination of the Néel vector in a CuMnAs thin-film antiferromagnet, *Nat. Photonics* **11**, 91 (2017).
- [26] S. Reimers, Y. Lytvynenko, Y. R. Niu, E. Golias, B. Sarpi, L. S. I. Veiga, T. Denneulin, A. Kovács, R. E. Dumini-Borkowski, J. Bläßer, M. Kläui, and M. Jourdan, Current-driven writing process in antiferromagnetic Mn<sub>2</sub>Au for memory applications, *Nat. Commun.* **14**, 1861 (2023).
- [27] P. Zhang, J. Finley, T. Safi, and L. Liu, Quantitative study on current-induced effect in an antiferromagnet insulator/Pt bilayer film, *Phys. Rev. Lett.* **123**, 247206 (2019).
- [28] L. Baldrati, C. Schmitt, O. Gomonay, R. Lebrun, R. Ramos, E. Saitoh, J. Sinova, and M. Kläui, Efficient spin torques in antiferromagnetic CoO/Pt quantified by comparing field- and current-induced switching, *Phys. Rev. Lett.* **125**, 077201 (2020).
- [29] C. C. Chiang, S. Y. Huang, D. Qu, P. H. Wu, and C. L. Chien, Absence of evidence of electrical switching of the antiferromagnetic Néel vector, *Phys. Rev. Lett.* **123**, 227203 (2019).

- [30] H. Meer, F. Schreiber, C. Schmitt, R. Ramos, E. Saitoh, O. Gomonay, J. Sinova, L. Baldrati, and M. Kläui, Direct imaging of current-induced antiferromagnetic switching revealing a pure thermomagnetoelastic switching mechanism in NiO, *Nano Lett.* **21**, 114 (2021).
- [31] W. L. Roth, Magnetic structures of MnO, FeO, CoO, and NiO, *Phys. Rev.* **110**, 1333 (1958).
- [32] S. I. Csiszar, M. W. Haverkort, Z. Hu, A. Tanaka, H. H. Hsieh, H.-J. Lin, C. T. Chen, T. Hibma, and L. H. Tjeng, Controlling orbital moment and spin orientation in CoO layers by strain, *Phys. Rev. Lett.* **95**, 187205 (2005).
- [33] J. Zhu, Q. Li, J. X. Li, Z. Ding, J. H. Liang, X. Xiao, Y. M. Luo, C. Y. Hua, H.-J. Lin, T. W. Pi, Z. Hu, C. Won, and Y. Z. Wu, Antiferromagnetic spin reorientation transition in epitaxial NiO/CoO/MgO(001) systems, *Phys. Rev. B* **90**, 054403 (2014).
- [34] M. J. Grzybowski, C. F. Schippers, M. E. Bal, K. Rubi, U. Zeitler, M. Foltyn, B. Koopmans, and H. J. M. Swagten, Electrical switching of antiferromagnetic CoO | Pt across the Néel temperature, *Appl. Phys. Lett.* **120**, 122405 (2022).
- [35] M. Yang, Q. Li, T. Wang, B. Hong, C. Klewe, Z. Li, X. Huang, P. Shafer, F. Zhang, C. Hwang, W. S. Yan, R. Ramesh, W. S. Zhao, Y. Z. Wu, X. Zhang, and Z. Q. Qiu, Current switching of the antiferromagnetic Néel vector in Pd/CoO/MgO(001), *Phys. Rev. B* **106**, 214405 (2022).
- [36] J. Xu, M. Jia, C. Zhou, Q. Li, P. Shafer, G. Chen, M. Yang, A. T. N'Diaye, E. Arenholz, Z. Qiu, and Y. Wu, Positive spin Hall magnetoresistance in single-crystalline Pt/CoO(001) bilayers, *Phys. Rev. B* **106**, 134425 (2022).
- [37] Q. Li, T. Gu, J. Zhu, Z. Ding, J. X. Li, J. H. Liang, Y. M. Luo, Z. Hu, C. Y. Hua, H.-J. Lin, T. W. Pi, C. Won, and Y. Z. Wu, Multiple in-plane spin reorientation transitions in Fe/CoO bilayers grown on vicinal MgO(001), *Phys. Rev. B* **91**, 104424 (2015).
- [38] C. Schmitt, A. Rajan, G. Beneke, A. Kumar, T. Sparmann, H. Meer, B. Bednarz, R. Ramos, M. A. Niño, M. Foerster, E. Saitoh, and M. Kläui, Mechanisms of electrical switching of ultrathin CoO/Pt bilayers, *Nano Lett.* **24**, 1471 (2024).